PCCP

Accepted Manuscript

ROYAL SOCIETY OF CHEMISTRY

www.rsc.org/pccp

Hydrogenation of Pt/TiO_2 {101} Nanobelts: A driving force for the improvement of methanol catalysis

Feila Liu[1], Peng Xiao[1,3], Wei Quan Tian[1], Ming Zhou[1], Yanhong Li[3], Xun Cui[1], Yunhuai Zhang[1]* , Xin Zhou[2]*

1 College of Chemistry and Chemical Engineering, Chongqing University, Chongqing 400044, P. R. China

2 Institute of Theoretical and Simulational Chemistry, Academy of Fundamental and Interdisciplinary Sciences, Harbin Institute of Technology, Harbin 150080, P. R. China

3 College of Physics, Chongqing University, Chongqing 400044, P. R. China

Authors: Feila Liu, E-mail: liufeila@u.washington.edu

Peng Xiao, E-mail: xiaopeng@cqu.edu.cn

Wei Quan Tian, E-mail: tianwq@cqu.edu.cn

Ming Zhou, E-mail: Zhoumingcqu2007@163.com

Yanhong Li, E-mail: lilymwj@gmail.com

Xun Cui, E-mail: cuixun212@163.com

*Corresponding author:

Yunhuai Zhang, E-mail: xp2031@163.com (Y. H. Zhang) Tel: +86 13883077781

Xin Zhou, E-mail: zhoux@hit.edu.cn (X.Zhou) Tel: +86 451-86403305

Abstract

Single-crystalline anatase TiO_2 nanobelts with dominant surface of {101} facet were hydrogenated and used as a substrate of platinum for methanol oxidation reaction (MOR). The hydrogenated TiO_2 anatase {101} supporting Pt exhibits a 228% increase of current density for methanol oxidation compared with the same system without hydrogenation in dark condition. The synergetic interactions of hydrogenated anatase {101} with Pt cluster were investigated through first principle calculations, and found that the hydrogenation shifts the conduction band minimum to the Fermi level of pristine TiO_2, and reduces the activation barrier for methanol dissociation considerably. Thus, this work provides an experimental and theoretical basis for developing non-carbon substrate with high electro-catalytic activity toward MOR.

Keywords TiO_2 nanobelts, hydrogenation, first principle calculations, platinum, methanol catalysis

1. Introduction

Direct methanol fuel cell (DMFC) is a promising candidate for using as a substitute power source in portable applications due to its high efficiency and low emission of pollutants. [1] Until now, Pt-based catalysts are highly regarded as the most suitable electrode materials for DMFC because of their high activity and stability.[2-4] Recently, some active catalytic oxide supports (non-carbon materials) garner significant attention because the substrate-platinum interactions can substantially influence the catalysts and catalytic pathway, [5,6] such as RuO_2, [7] SnO_2, [8] WO_3, [9,10] TiO_2 [11,12] and SiO_2.[13,14] Among of those oxides, TiO_2 is regarded as a classic non-carbon substrate that exhibits strong metal support interaction (SMSI). [15-19] The strong interaction between TiO_2 and platinum that facilitates the MOR has been confirmed through a series of theoretical calculations [17,20,21] and experimental verifications. [11,12,22-24] However, most of those studies were focused on pure TiO_2. As catalyst support, the pure TiO_2 is generally not preferred in electrode applications because of its low conductivity and insufficient catalysis.

Currently, modified TiO_2 has gained considerable attention in photocatalytic area through adding controlled metals [25, 26] or nonmetal impurities. [27-30] Particularly, the introduction of nonmetallic light-element dopants, such as hydrogen, [31-33] has triggered extensive research interest. Experimentally, Chen et al. reported the enhanced photocatalytic water splitting performance of 'black titania' in the visible light and near-infrared region, which was obtained from TiO_2 anatase nanoparticles that were treated in a H_2 atmosphere. [31] Wang et al. demonstrated that annealing rutile

TiO_2 nanowire arrays in a H_2 atmosphere created oxygen vacancy sites thus forming donor states below the conduction band. [32] This improves the light absorption and charge transport of TiO_2 similar to n-type doping, which enhances the performance of water oxidation performance. Theoretically, Gao et al investigated the mechanism for the improvement of photocatalytic performance induced by doping of hydrogen. [34] Their calculations revealed that the n-type TiO_2 was formed by the introduction of hydrogen interstitial or substitution. Despite the above works in photocatalytic area, few studies focus on synergistic effects of hydrogen modified TiO_2 materials and platinum for MOR and the underlying catalytic mechanism is not well understood.

It is well known that the catalytic activity of TiO_2 crystals is heavily dependent upon the surface structure (surface atomic arrangement and coordination). [35-38] For instance, by investigating a set of anatase crystals with predominant {001}, {101}, or {010} facets of TiO_2, {101} surface exhibits higher reactivity than {001} in photooxidation reactions for OH radical generation and photoreduction for hydrogen evolution.[39, 40] Thus, in the present work, TiO_2 substrate with low-index anatase {101} surface was prepared and hydrogenated for loading Pt. We demonstrated that the hydrogenated TiO_2 anatase {101} supporting Pt has more significant catalytic activity (a 228% increase of current density for methanol oxidation) than the same system without hydrogenation in the dark condition. Meanwhile, to understand the catalytic mechanism, a density functional theory (DFT) based method in conjunction with the projector augmented wave and pseudopotential methods have been applied to study the hydrogen interstitial anatase {101} supporting Pt. To our knowledge, it is the first

time to combine experimental investigation with computational simulation to explore the hydrogenated TiO_2 {101} loading Pt for methanol electro-catalysis. The present work is expected to provide experimental and theoretical assistance for understanding the synergistic catalytic mechanism of MOR in the non-carbon material supporting Pt electro-catalysts.

2. Experimental section

2.1 Preparation of hydrogenated TiO_2

TiO_2 nanobelts were prepared by hydrothermal treatment.[41] The commercial titanium dioxide powder was added into a 10 M NaOH aqueous solution in a Teflon-lined stainless steel autoclave. The autoclave was sealed and subsequently heated at 200 °C for 24 hours. After hydrothermal processing, white fluffy product was washed with deionized water and 0.1 M hydrochloric acid until the pH of the washing solution is reduced to ≤7. The as-washed samples were then calcinated at 700 °C for 30 minutes at a ramp rate of 1 °C/min in the air and hydrogen (H_2/Ar 5% vol), respectively. The hydrogenated TiO_2 is denoted as H-TiO_2 hereafter.

2.2 Preparation of Pt/TiO_2 electrode

The prepared TiO_2 nanobelts were coated on Titanium foil with a 1.0 cm^2 geometric area through an electrophoretic deposition (EPD) process. Pt nanoparticles were deposited on the different TiO_2 substrates by pulsed electrodeposition method.[22] The electrodeposition was carried out in a conventional three-electrode cell, the TiO_2/Ti served as the working electrode, an Ag/AgCl electrode and a Pt foil electrode served as the reference and counter electrode, respectively. The deposition bath was

$H_2PtCl_6 \cdot 6H_2O$ (1 g L−1) at 50 ◦C and pH = 1. The Pt deposition was prepared at the constant current density with a quantity of electricity of 1.5mC cm^{-2}.

2.3 Physical characterization and electrochemical measurements

The morphology, phase structure and surface chemical states of the as-prepared TiO_2 were investigated by field emission scanning electron microscopy (FESEM, Nova 400 Nano-SEM), X-ray diffraction (XRD, Shimadzu ZD-3AX,Cu Kα radiation) and X-ray photoelectron spectroscopy (XPS,ESCALAB 250 Thermo Fisher Scientific), respectively. The crystal structure of the as-prepared TiO_2 was characterized by high resolution transmission electron microscopy (HRTEM) and selected area electron diffraction (SAED) (a 200 kV Tecnai G2 F20 TEM apparatus). The chemical composition of the as-prepared samples was analyzed by energy dispersive X-ray spectroscopy (EDS, TESCAN VEGAII, at 20 kV). CHI600C electrochemical work station (Shanghai, China) was employed for the electrochemical measurements in 1 M NaOH solution with/without 0.5 M CH_3OH respectively, which were carried out in a conventional three electrode electrochemical cell. The as-prepared sample with a geometric area of 1.0 cm^2 was placed as the working electrode, and Pt foil and Ag/AgCl (saturated KCl) were used respectively as the counter and reference electrodes. All the experiments were performed at room temperature and in dark condition.

3. DFT calculations

The anatase {101} crystallographic surface was built in accordance with our previous study. [17] The Vienna *ab initio* simulation package (VASP) [42,43] with the

projector augmented wave method (PAW) [44] and PBE functional [45] were used for all calculations. All other parameters, including cutoff energy, lateral dimension of the surface unit cell, and the number of TiO_2 layers, were kept consistent with our previous study. [17] The atoms in the lower half of the slab were fixed at their bulk positions and the top half atoms of the slab with the adsorbed Pt_6 cluster were allowed to relax according to the calculated forces. Accordingly, the initial geometries were partially relaxed to the nearest local minimum structure. The electronic structures of TiO_2 with and without hydrogenation were treated by PBE+U method with the Hubbard on-site Coulomb interaction parameter (U-J). A large value of the U-J (7.0 eV) is used due to a good agreement of the calculated bandgap with experimental data in previous work. [34] The transition-state structures for the initial bond-breaking step of methanol dissociation were determined by the nudged elastic band (NEB) method. [46,47]

4. Results and discussion

4.1. Structural and chemical compositional characterization

When the TiO_2 nanostructure was deposited on the Ti foil through EPD process, a uniform film with thickness of about 3 microns was obtained, as shown in the cross-section SEM image of Fig. 1(a). The morphology of the synthesized TiO_2 nanostructure is shown in Fig. 1 (b). The TiO_2 shows nanobelts structures which are 60–300 nm wide and several microns long. Pt nanoparticles were deposited on the TiO_2 film by pulsed electrodeposition method. EDS (Fig. 1 (C)) measurement demonstrates that the Pt nanoparticles are distributed on the TiO_2 film.

The structure of the TiO_2 nanobelts was investigated with x-ray diffraction (XRD). The as-synthesized titania nanostructure exhibits the monolithic anatase phase, as confirmed by the XRD patterns (black curve in Fig. 3 (b)). The pure TiO_2 nanocrystals are highly crystallized, as seen from the well-resolved lattice features shown in the HRTEM image (Fig. 2 (b)). The HRTEM measurements and the selected area diffraction (SAD) patterns (Fig. 2(c)) show an identical lattice spacing (d = 0.35 nm typical of anatase). The size of a single nanobelt (Fig. 2 (a)) is approximately 250 nm in diameter. The TEM image shown in Fig. 2 (a) reveals that the dimension of the nanobelt is well in agreement with the SEM observation. Electron diffraction data indicate that the nanobelts are single crystalline anatase TiO_2. The relative rotation between the diffraction pattern and the image is corrected and [010] is believed to be the growth direction of the nanobelts. This is supported by the high resolution TEM image in Fig. 2(b), where the lattice fringes are perpendicular to the growth direction, as well as the schematic illustration of the relation between the incident beam and the nanobelt during recording the images and diffraction patterns in Fig. 2(d). In addition, according to the calculation results predicted in literature,[41] the crystallographic plane of the major exposed surface of the nanobelts is determined to be {101} facet, which is the most thermodynamically stable crystal facet of anatase TiO_2.[19]

Fig. 3 (a) shows the color difference of TiO_2 after hydrogenation. Clearly, after an additional reduction treatment in H_2/Ar, the powder turns white to dark grey. Strong XRD peaks ((red curve in Fig. 3 (b)) correspond to well crystallized anatase after

hydrogenation, and no obvious change of morphology of the hydrogenated nanostructures is observed from our SEM data.

With X-ray photoelectron spectroscopy (XPS), the change of surface chemical bonding of TiO_2 nanobelts due to hydrogenation was examined. The O 1s XPS spectra of the air and hydrogen treated TiO_2 nanobelts show a slight difference (Fig. 4 (a)), and both samples exhibit the peak of 529.9 eV that corresponds to the characteristic Ti−O−Ti. Other peaks centered at 531.8 and 532.0 eV are attributed to Ti−OH species, which has been reported to be located at the binding energy of ~2.0eV higher than the peak of Ti-O-Ti. [48,49] However, for the H-treated TiO_2, the spectrum is split into three peaks. The broader peak at 534.6 eV can be attributed to hydroxyl groups after hydrogenation. In Fig 4 (b), two broad peaks centered at ~464.3 and ~458.6 eV corresponding to the characteristic Ti 2p1/2 and Ti 2p3/2 peaks of Ti^{4+} are observed for air-TiO_2. [50] In comparison to air−TiO_2, the peaks of the H−TiO_2 sample show a slight shift to low binding energy, indicating of possibly different bonding enviroments. Moreover, from XPS, no significant variation in the composition of the samples treated in air and H_2/Ar was observed. There is no massive conversion to a suboxide phase occurred in the surface-near region (penetration depth of XPS ≈5−10 nm) according to XPS and XRD combined analysis.

The UV−vis absorption spectra in Fig. 5 (a) for air treated and hydrogen treated samples is notably different. In the hydrogenation case, this process (dark grey TiO_2, red line) induces the red-shift of the UV absorption threshold and a high absorption in the visible region. Based on the absorption spectra, the optical bandgaps were

calculated by the Tauc equation.[51] As shown in the inset of Fig. 5 (a), the Tauc plots point to a band gap of 2.98 eV for the air annealed TiO_2 and 2.87 eV for the hydrogenated TiO_2. Apparently, the hydrogenation effect can effectively narrow the bandgap of TiO_2.

Structural properties of TiO_2 nanobelts were further examined by measuring Raman scattering. Analysis was carried out also on hydrogenated TiO_2 that has the same phase composition. Five ($3E_g$ + B_{1g} + A_{1g}) Raman-active modes of anatase phase were detected in both samples (Fig. 5 (b)).[52] Distinctly，a blue-shift and broadening of the most intensive E_g peak were observed in the hydrogenated TiO_2. It is known that annealing in a reductive environment will create some point defects in the TiO_2 crystal structure and further lead to structural disorder: the interaction between TiO_2 host matrix and hot H_2 molecule gives rise to V_O's (vacancy of oxygen) that overcome the activation energy of TiO_2 lattice rearrangement and accelerate it.[53]

In order to reveal the existence of oxygen vacancy after hydrogenation, the photoluminescence (PL) emission was measured as well. Fig. 5 (c) shows the comparison of PL spectra of pristine and hydrogenated TiO_2 in the wavelength range of 350−550 nm with the excitation at 300 nm. The PL emission intensity of H-TiO_2 at 388 is only half of the air-TiO_2, which indicates that the recombination rate of electrons and holes is inhibited considerably in H-TiO_2 because of the formation of oxygen vacancies during the hydrogenation. The oxygen vacancies actually serves as electron capture traps, hence separate the charge carriers and reduces the recombination significantly. Hence, the localized defects associated with V_O's is

responsible for the blue-shift and broadening of the peak observed in the hydrogenated TiO_2 (see position and FWHM in inset of Fig. 5 (b)).

4.2. Electrochemical measurements

The electrocatalytic activity of different Pt/TiO_2 electrodes toward methanol oxidation reaction was further studied. All the tests were carried out in alkaline media and dark condition. For comparison, commercial TiO_2 powder was also fabricated to a film by EPD method and deposited with the same amount of Pt. Fig. 6 shows their CVs in solution of 1.0 M NaOH aqueous solution (a) and 1.0 M NaOH aqueous solution containing 0.5 M methanol (b) at a scan rate of 50 mV s^{-1} respectively. Usually, current density and onset potential of methanol oxidation are two important parameters used to evaluate the performance of electro-catalysts. However, from Fig. 6(a) and (b), all the electrodes do not show significant difference in the onset of methanol oxidation potential. As shown in Fig. 6(b), the peak current densities of the reaction on Pt/TiO_2, Pt/commercial TiO_2 and Pt/H-TiO_2 are 21.1, 40.0 and 69.2 $mA.cm^{-2}$, respectively. On comparison of these three electrodes, it is clear that Pt/H-TiO_2 has a significant enhancement of the current density in the electro-oxidation. Meanwhile, the peak potential of Pt/H-TiO_2 presents a significant shift to more anodic (from -0.24 to 0.09 eV) after hydrogenation, which illustrates that the potential range of the electro-oxidation for methanol increases. In addition, Pt/commercial TiO_2 electrode shows a relatively noticeable response to CH_3OH under the same condition. The improved catalytic activity which is higher than Pt/TiO_2 can be attributed to the multi-crystal surface of commercial TiO_2.

The electro-catalytic stability of the different Pt/TiO_2 electrodes for methanol in alkaline media was investigated by amperometric method and the corresponding I–t curves are shown in Fig. 6 (c). All these electrodes show rapid current density decay within the first 100 seconds, followed by a nearly constant current density for the rest 1400 seconds. Obviously, the ultimate steady current density on the Pt/H-TiO_2 electrode is larger than that on the Pt/TiO_2 or Pt/commercial TiO_2 electrode for methanol oxidation in alkaline media. The blocking of the surface with CO_{ad} species and the time dependent adsorption of the strongly bound irreversible OH_{ad} species in alkaline media are responsible for the current density decay. [54,55]

In order to analyze the electrochemical processes (such as electron transport property) occurring at the solution/electrode interface, EIS was employed to probe the features of electrodes. Fig. 6(d) shows the EIS spectra (Nyquist plots, corresponding to the imaginary part Z' vs the real part Z " of the complex impedance Z) of the three electrodes measured in a mixed solution of 1M NaOH and 0.5 M CH_3OH. Usually, the semicircle diameter corresponds to the electron transfer resistance controlling the kinetics at the electrode interface. [56] As shown in Fig.6(d), the semicircle diameter for the Pt/H-TiO_2 electrode is smaller than that for Pt/air TiO_2 electrode by fitting the curves, suggesting that the electron-transfer resistance of Pt/H-TiO_2 electrode reduces and the interfacial charge transfer between the adsorbed methanol molecules and catalyst support increases.

In summary, all the above data reveal that as-prepared Pt/TiO_2 possesses better electrocatalytic activity and stability for methanol electro-oxidation after

hydrogenation.

4.3 Hydrogenation mechanism

To understand the effects of hydrogen on the electronic properties of Pt/TiO_2, we constructed perfect TiO_2, oxygen vacancy-TiO_2 (V_O-TiO_2), and hydrogenated TiO_2 (H-TiO_2) anatase {101} surface respectively (Fig.7 (a) and (b)). The surface oxygen vacancy on anatase TiO_2 {101} was created by removing a surface 2cO atom. The original 6cTi and 5cTi atoms bonding to the 2cO atom at the vacancy site become five- and four-coordinated atoms, denoted as 5cTi(d) and 4cTi(d), respectively, as shown in Fig.7(b). Based on this oxygen vacancy model, subsequently, interstitial hydrogen atom was introduced, forming a surface disorder. Gao et al. [34] designed two possible nonequivalent sites for an interstitial hydrogen atom bonded to oxygen and proved that the hydrogen atom bonded perpendicularly to the Ti-O-Ti plane was the most stable. Thereupon, an interstitial hydrogen atom bonded perpendicularly to the surface Ti-O-Ti plane was considered in the present work, as shown in Fig. 7(b). When H acts as a donor, the H atom bonds to the O neighboring site in this impurity configuration and forms a 0.8 Å O-H bond. The extra electron introduced by H is completely delocalized. Bader charges analysis confirms this finding (see Table 1).

To clearly reveal the effects of hydrogen on the electronic properties of TiO_2, the density of states (DOS) were determined (depicted in Fig. 8). In Fig. 8(a), the calculated bandgaps are 2.50, 2.46 and 2.00 eV for perfect TiO_2, V_O-TiO_2, and H-TiO_2, respectively. Clearly, the surface disorder induces a remarkable bandgap narrowing. Furthermore, V_O's introduce localized states at 1.08~1.17 eV below the

conduction band minimum (CBM) of V_O-TiO_2. More interestingly, the Fermi level moves in the original conduction band after hydrogen interstitial. This is consistent with the observation reported in literature, [34] in which the interstitial hydrogen leads to n-type TiO_2, and can explain why electron-transfer resistance of hydrogenated TiO_2 reduces in Fig.6 (d). Similarly, for H-TiO_2, a mid-gap state (−1.28 ~−0.84 eV) appears as a result of the introduction of hydrogen impurities. Hydrogenation is considered as driving force inducing n-type conductivity in TiO_2. The partial density of states (PDOS) in Fig. 8(b) shows the valence band maximum (VBM) and CBM states mainly come from the contribution of the O p and Ti d electrons. The s electrons of hydrogen are almost negligible, which further confirmed the extra electron introduced by H is completely delocalized or transferred to heavy atoms.

Adsorption of Pt on the anatase {101} is considered as well in our work. Several possible six-atom Pt cluster conformations were relaxed and two most stable conformations adsorbing on pure and hydrogenated anatase {101} are presented in Fig. 9 (a) and (b). As depicted in Fig. 9 (a) and (b), the Pt clusters form two similar 3D double quadrangular adsorption structures. Adsorption energies and clustering energies for the Pt sexamers on different TiO_2 surface were summarized in Table 1. For the case of Pt/H-TiO_2, E^{ads} and E^{clu} are slightly lower than those on perfect TiO_2, slight decrease of E^{ads} and E^{clu} values indicates that the presence of hydrogen does not stabilize the Pt clusters adsorbed on the TiO_2 surface. As shown in Table 1, the Pt cluster in the Pt_6/TiO_2 is positively charged as it losses 0.25e upon adsorption; while in Pt_6/V_o-TiO_2, the Pt cluster gains 0.37e. For the Pt_6/H-TiO_2 configuration, the Pt

cluster gains 0.44e, while the H atom is positively charged (0.63). It is evident that hydrogen atom transfers more electrons to Pt cluster and an OH bond is subsequently formed. [57] Charge transfer may enhance chemical activity of Pt cluster. To further expound upon this point of view, condensed Fukui function was calculated to predict the site reactivity (regioselectivity) of Pt clusters (Table 2).

Table 1 Adsorption and clustering energies (eV) of Pt cluster adsorbed on pure and hydrogenated anatase and Bader charge of Pt and H atoms. The subscripts on Pt indicate the numbering as labeled in Figure 9 (a) and (b).

Structures	**Energy**(eV)		**Bader Charge** (|e|)						
	E^{ads}	E^{clu}	H	Pt_1	Pt_2	Pt_3	Pt_4	Pt_5	Pt_6
Pt_6/TiO_2	6.48	4.42	—	0.04	0.14	-0.10	-0.10	0.23	0.04
Pt_6/V_O-TiO_2	5.33	4.30	—	-0.55	0.14	-0.15	-0.09	0.20	0.08
Pt_6/H-TiO_2	6.33	4.33	0.63	-0.61	0.10	-0.14	-0.10	0.21	0.10

The condensed Fukui function measures the linear response of the electron density to charge transfer from an approaching reagent [58] and was calculated as follows, [59]

$$f_N^+(\mathrm{r}) = (\partial \rho(\boldsymbol{r})/\partial \mathrm{N})^+_{\upsilon(r)} = \rho_{N+1}(\boldsymbol{r}) - \rho_N(\boldsymbol{r}) \qquad (1)$$

$$f_N^-(\mathrm{r}) = (\partial \rho(\mathbf{r})/\partial \mathrm{N})^-_{\upsilon(r)} = \rho_{\mathrm{N}}(\mathbf{r}) - \rho_{\mathrm{N-1}}(\mathbf{r}) \qquad (2)$$

where $\rho_{N+1}(\mathbf{r})$, $\rho_N(\mathbf{r})$, and $\rho_{N-1}(\mathbf{r})$ are the electron densities of the N+1, N, and N–1 electron systems evaluated at the geometry of N, respectively. A large $f_N^+(\mathrm{r})$ value indicates high nucleophilic reactivity at r, and a large $f_N^-(\mathrm{r})$ value specifies high electrophilic reactivity at r. [60] From Table 2, in the case of Pt_6/TiO_2, Pt3 atom has the largest $f_N^+(\mathrm{r})$ and $f_N^-(\mathrm{r})$ values among all the atoms, indicating that the Pt_6 cluster is

susceptible to nucleophilic and electrophilic attack at the Pt3 site. The Pt3 atom in the Pt_6/H-TiO_2 possesses a higher chemical activity compared to its counterpart in the Pt_6/TiO_2, suggesting that the presence of hydrogen enhances the reactivity of the metallic cluster.

Table 2 Condensed Fukui function f_N^+ (r) and f_N^- (r) for perfect and hydrogenated Pt_6/TiO_2.

Atom Configurations	Pt_1	Pt_2	Pt_3	Pt_4	Pt_5	Pt_6
f^+ -Pt_6/TiO_2	0.05	0.04	0.08	0.08	0.04	0.04
f^- -Pt_6/TiO_2	0.06	0.07	0.09	0.08	0.07	0.07
f^+ -Pt_6/H -TiO_2	0.07	0.06	0.10	0.09	0.07	0.07
f^- -Pt_6/H -TiO_2	0.08	0.07	0.10	0.09	0.07	0.06

Ge et al.[20] found that there is a very weak interaction between hydrogen atoms or oxygen atom (from either a methyl group or hydroxyl group of a methanol molecule) with anatase substrate, hence, only methanol adsorption on the metallic cluster is considered here. Additionally, as revealed by the Fukui function analysis, the Pt3 atom in the both Pt_6/TiO_2 and Pt_6/H-TiO_2 possesses a higher chemical activity than the Pt atoms in other sites; therefore, the following analysis will only focus on the reaction between the methanol molecule and Pt3 atom, as illustrated in Fig. 10.

To quantify the H effect on bond-breaking of methanol, potential energy profiles (PEP) for C-H breaking in the process of methanol dissociation over Pt_6/TiO_2 and Pt_6 /H-TiO_2 were shown in Fig. 10. For Pt_6/TiO_2, the C-H, C-O, and O-H bond activation barriers are 0.35, 0.84 and 0.59 eV, respectively (see Fig. 10 (b)); for Pt_6/H-TiO_2, the activation barriers of the C-H, C-O, and O-H bonds are 0.13, 0.69 and

0.27 eV, respectively (see Fig. 10 (a)). This is in direct contrast to the dissociative adsorption of methanol on Pt_6/TiO_2 and $Pt_6/H\text{-}TiO_2$, where C-H bond scission over $Pt_6/H\text{-}TiO_2$ is more favorable. On the surface of Pt_6/TiO_2, the C-H bond activation barrier is 0.35 eV, however that in the pathway of the indirect dissociation is 0.13 eV for the $Pt_6/H\text{-}TiO_2$, which is 0.22 eV lower than that on the Pt_6/TiO_2. The adsorption of CH_3OH is exothermic and it releases more energy in the Pt_6/TiO_2 profile. However, this cannot explain the improved performance of $Pt_6/H\text{-}TiO_2$ on MOR, *i.e.* this adsorption is not the rate-determining step. According to the PEP, the adsorbed intermediate is relatively stable as it must go through a transition state to achieve C-H bond breaking. The activation barrier for C-H breaking in the $Pt_6/H\text{-}TiO_2$ reaction is clearly lower than that in the Pt_6/TiO_2, and this favorable activation energy barrier rationalizes the improved performance of $Pt_6/H\text{-}TiO_2$. This conclusion coincides well with Fukui function analysis. This is also in accordance with the electrochemical measurement result of $Pt/H\text{-}TiO_2$ electrode in the mixed solution of NaOH and methanol, as shown in Fig. 6(b).

5. Conclusions

In the present work, experiments demonstrate that hydrogenation significantly improves the electrochemical performance of Pt/TiO_2 for methanol oxidation**,** and significantly influence the synergistic catalytic effect of TiO_2 with Pt. First principles calculations on electronic properties of the low-index anatase {101} surface reveals that hydrogen incorporation not only leads to the narrowing of the band-gap of TiO_2, but also induces mid-gap states in the material which improves the electron capture

capacity. Condensed Fukui function analysis reveals that the Pt cluster adsorbed on H-TiO_2 possesses a higher chemical activity. The reduced activation barrier for methanol dissociation via C-H bond breaking on Pt_6/H-TiO_2 is responsible for the improved catalytic activity of Pt_6/H-TiO_2 over Pt_6/TiO_2.

The present findings imply that an optimal H_2 treatment of anatase TiO_2 {101} can trigger considerable intrinsic catalytic activity, which possibly can be exploited for much wider applications. The hydrogenation mechanism could also provides a theoretical basis for further study on other non-carbon material loading Pt electro-catalysts toward MOR.

Acknowledgements

This research was financially supported by Chongqing University Postgraduates' Innovation Project, the National Natural Science Foundation of China (No:21303030). WQT thanks the support from the Open Project of State Key laboratory of Supramolecular Structure and Materials (JLU) (SKLSSM2015018).

Reference

1 R. Dillon, S. Srinivasan, A. S. Aricò and V. Antonucci, *J. Power Sources*, 2004, **127**, 112–126.

2 O. A. Petrii, *J. Solid State Electrochem.*, 2008, **12**, 609–642.

3 Y. P. Sun, L. Xing and K. Scott, *J. Power Sources*, 2008, **195**, 1–10.

4 C. X. Xu, R.Y. Wang, M. W. Chen, Y. Zhang and Y. Ding, *Phys. Chem. Chem. Phys.*, 2010, **12**, 239–246.

5 P. C. Biswas and M. Enyo, *J. Electroanal. Chem.*, 1992, **322**, 203–220.

6 C. R. Henry, *Surf. Sci. Rep.*, 1998, **31**, 235–325.

7 S.Y. Huang, C. M. Chang, K.W. Wang and C.T. Yeh, *Chem. Phys. Chem.*, 2007, **8**, 1774–1777.

8 A. Aramata, I. Toyoshima and M. Enyo, *Electrochim. Acta*, 1992, **37**, 1317–1320.

9 D.Y. Zhang, Z. F. Ma, G. Wang, K. Konstantinov, X. Yuan and H. K. Liu, *Solid State Lett.*, 2006, **9**, A423–A426.

10 K.W. Park, Y. E. Sung and M. F. Toney, *Electrochem. Commun.*, 2006, **8**, 359–363.

11 K. Hirakawa, M. Inoue and T. Abe, *Electrochim. Acta*, 2010, **55**, 5874–5880.

12 H. C. He, P. Xiao, M. Zhou, F. L. Liu, S. J. Yu, L. Qiao and Y. H. Zhang, *Electrochim. Acta*, 2013, **88**, 782–789.

13 A. K. Santra, B. K. Min and D.W. Goodman, *Surf. Sci.*, 2002, **515**, L475–L479.

14 J. B. Giorgi, T. Schroeder, M. Baumer and H. J. Freund, *Surf. Sci.*, 2002, **498**, L71–L77.

15 S. J. Tauster, *Acc. Chem. Res.*, 1987, **20**, 389–394.

16 G. L. Haller and D. E. Resasco, *Adv. Catal.*, 1989, **36**, 173–235.

17 F. L. Liu, P. Xiao, E. Uchaker, H. C. He, M. Zhou, X. Zhou and Y. H. Zhang, *Appl. Surf. Sci.*, 2014, **315**, 81–89.

18 M. Lazzeri, A. Vittadini and A. Selloni, *Phys. Rev. B*, 2002, **65**, 119901.

19 M. Lazzeri, A. Vittadini and A. Selloni, *Phys. Rev. B*, 2001, **63**, 155409-1–155409-9.

20 Y. Han, C. J. Liu and Q. F. Ge, *J. Phys. Chem. C*, 2009, **113**, 20674–20682.

21 Y. Han, C. J. Liu and Q.F. Ge, *J. Phys. Chem. B*, 2006, **110**, 7463–7472.

22 H. C. He, P. Xiao, M. Zhou, Y. H. Zhang, Y.C. Jia and S. J. Yu, *Catal. Commun.*, 2011, **16**, 140–143.

23 H. C. He, P. Xiao, M. Zhou, Y. H. Zhang, Q. Lou and X. Z. Dong, *Int. J. Hydrog. Energy*, 2012, **37**, 4967–4973.

24 C.T. Campbell and C. H. F. Peden, *Science*, 2005, **309**, 713–714.

25 M. R. Hoffmann, S.T. Martin, W. Choi and D.W. Bahnemann, *Chem. Rev.*, 1995, **95**, 69–96.

26 W. Choi, A. Termin and M. R. Hoffmann, *Angew. Chem.*, 1994, **106**, 1148–1149.

27 R. Asahi, T. Morikawa, T. Ohwaki, K. Aoki and Y. Taga, *Science*, 2001, **293**, 269–271.

28 S. U. M. Khan, M. Al-Shahry and W.B. Ingler Jr., *Science*, 2002, **297**, 2243–2245.

29 X. B. Chen, C. Burda, *J. Am. Chem. Soc.*, 2008, **130**, 5018–5019.

30 S. Hoang, S. Guo, N. T. Hahn, A. J. Bard and C. B. Mullins, *Nano Lett.*, 2012, **12**,

26−32.

31 X. Chen, L. Liu, P. Y. Yu and S. S. Mao, *Science*, 2011, **331**, 746−750.

32 G. Wang, H. Wang, Y. Ling, Y. Tang, X. Yang, R. C. Fitzmorris, C. Wang, J. Z. Zhang and Y. Li, *Nano Lett.*, 2011, **11**, 3026−3033.

33 N. Liu, C. Schneider, D. Freitag, M. Hartmann, U. Venkatesan, J. Muller, E. Spiecker and P. Schmuki, *Nano Lett.*, 2014, **14**, 3309−3313.

34 H. Pan, Y. W. Zhang, V. B. Shenoy and H. J. Gao, *J. Phys. Chem. C*, 2011, **115**, 12224–12231.

35 P. A. M. Hotsenpiller, J. D. Bolt, W. E. Farneth, J. B. Lowekamp and G. S. Rohrer, *J. Phys. Chem. B*, 1998, **102**, 3216−3226.

36 C. L. Pang and G. Thornton, *Surf. Sci.*, 2006, **600**, 4405−4406.

37 T. Taguchi, Y. Saito, K. Sarukawa, T. Ohno and M. Matsumura, *New J. Chem.*, 2003, **27**, 1304−1314.

38 T. Ohno, K. Sarukawa and M. Matsumura, *New J. Chem.*, 2002, **26**, 1167−1170.

39 G. K. Mor, O. K. Varghese, M. Paulose, K. Shankar and C.A. Grimes, *Sol. Energ. Mat. Sol. C*, 2006, **90**, 2011−2075.

40 C. H. Cho, M. H. Han, D. H. Kim and D. K. Kim, *Mater. Chem. Phys.*, 2005, **92**, 104−111.

41 N.Q. Wu, J. Wang, D.N. Tafen, H. Wang, J. G. Zheng, J. P. Lewis, X .G. Liu, S.S. Leonard and A. Manivannan, *J. Am. Chem. Soc.*, 2010, **132**, 6679–6685.

42 G. Kresse and J. Hafner, *Phys. Rev. B*, 1993, **48**, 13115–13118.

43 G. Kresse and J. Furthmuller, *VASP*, the Guide, 2005.

44 G. Kresse and D. Joubert, *Phys. Rev. B: Condens. Matter Mater. Phys.*, 1999, **59**, 1758–1775.

45 J. P. Perdew, K. Burke and M. Ernzerhof, *Phys. Rev. Lett.*, 1996, **77**, 3865–3868.

46 G. Mills, H. Jonsson and G. K. Schenter, *Surf. Sci.*, 1995, **324**, 305–337.

47 G. Henkelman and H. Jonsson, *J. Chem. Phys.*, 2000, **113**, 9978–9985.

48 E. McCafferty and J. P. Wightman, *Surf. Interface Anal.*, 1998, **26**, 549–564.

49 X. H. Lu, D. Z. Zheng, T. Zhai, Z. Q. Liu, Y.Y. Huang, S. L. Xie and Y. X. Tong, *Energy Environ. Sci.*, 2011, **4**, 2915−2921.

50 M. S. Lazarus and T. K. Sham, *Chem. Phys. Lett.*, 1982, **92**, 670−674.

51 M. Q. Yang and Y. J. Xu, *J. Phys. Chem. C*, 2013, **117**, 21724−21734.

52 S. Santangelo, G. Messina, G. Faggio, A. Donato, L. De Luca, N. Donato, A. Bonavita and G. Neri, *J. Solid State Chem.*, 2010, **183**, 2451−2455.

53 M. Salari, K. Konstantinov and H. K. Liu, *Mater. Chem.*, 2011, **21**, 5128−5133.

54 X. He and C. Hu, *J. Power Sources*, 2011, **196**, 3119–3123.

55 A. V. Tripkovic, K. D. Popovic and J. D. Lovic, *Electrochimica Acta*, 2001, **46**, 3163–3173.

56 E. Frackowiak, G. Lota, T. Cacciaguerra and F. Beguin, *Electrochem. Commun.*, **2006**, 8, 129–132.

57 A. D. Panayotov and J. T. Yates, *Chem. Phys. Lett.*, 2007, **436**, 204–208.

58 L. J. Bartolotti and P. W. Ayers, *J. Phys. Chem. A*, 2005, **109**, 1146–1151.

59 R. G. Parr and W. Yang, *J. Am. Chem. Soc.*, 1984, **106**, 4049–4050.

60 P.W. Ayers and R. G. Parr, *J. Am. Chem. Soc.*, 2000, **122**, 2010–2018.

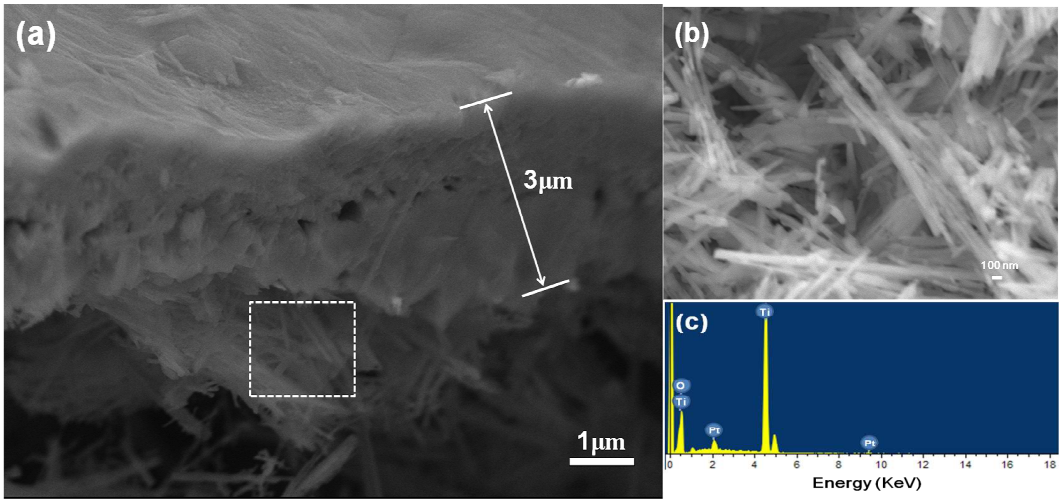

Figure 1 SEM images of (a) the TiO_2 film coated on Ti foil and (b) the synthesized pure TiO_2 nanobelts ; (c) EDS spectrum of Pt/TiO_2.

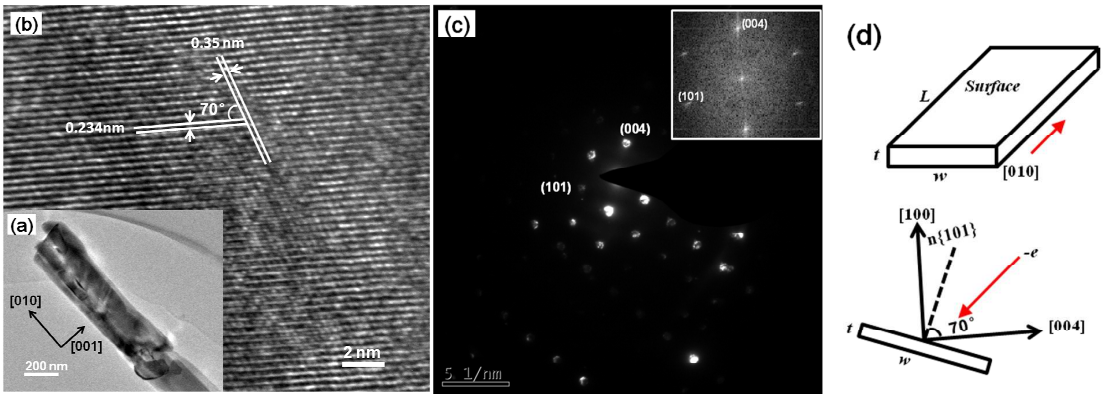

Figure 2 (a) TEM, (b) HR-TEM, and (c) SAED images of anatase TiO_2 nanobelts. The illustration in the Figure (c) is the fourier transformed pattern from Figure (b); (d) schematic illustrations of the nanobelt and the relation between the incident beam and the nanobelt during the images and diffraction patterns measurements.

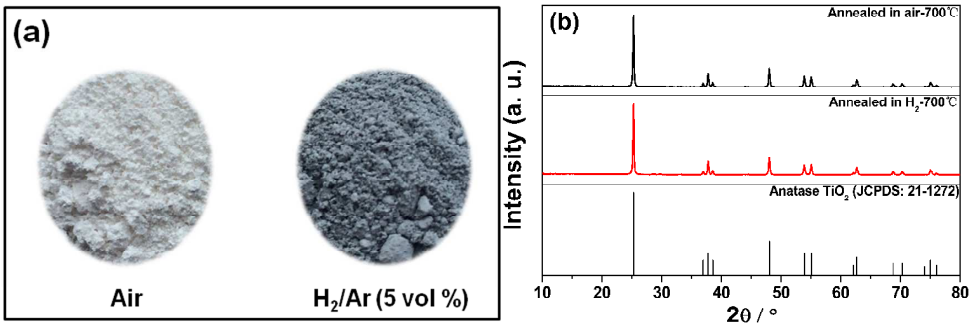

Figure 3 (a) Images of TiO_2 nanobelts powder annealed in air and H_2/Ar (5 vol %) at 700 °C, respectively; (b) XRD patterns of TiO_2 nanobelts annealed in different conditions.

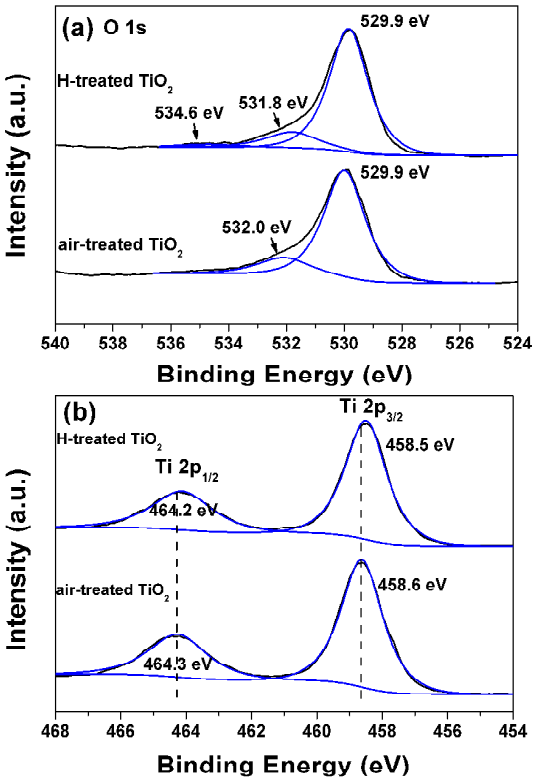

Figure 4 (a) O 1s core level XPS spectra of air–TiO_2 and H–TiO_2 nanobelts; (b) Ti 2p core level XPS spectra of air–TiO_2 and H–TiO_2 nanobelts. Black curves are the experimental data.

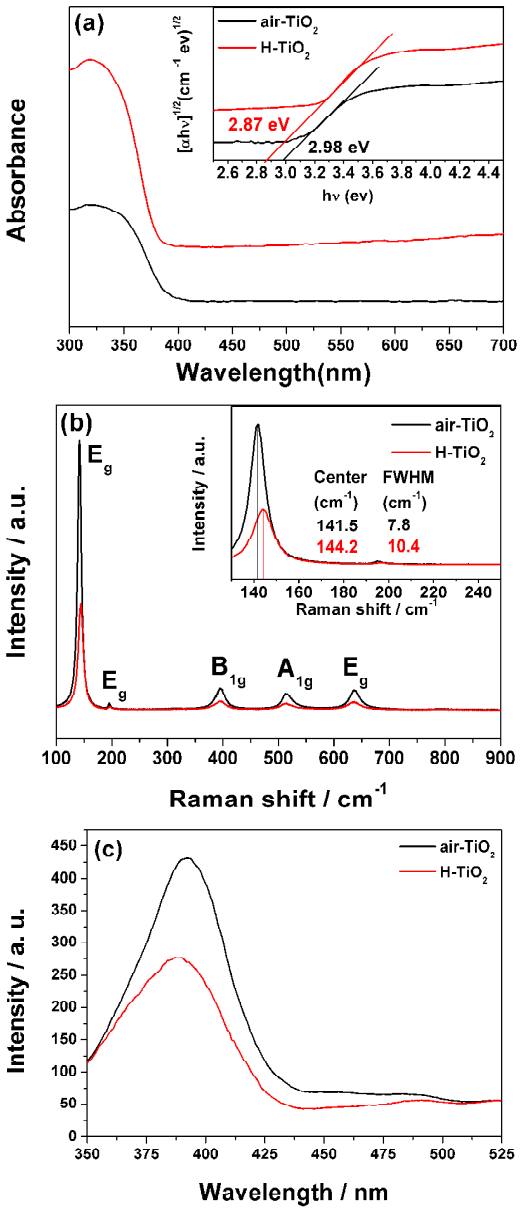

Figure 5 (a) UV−vis absorbance spectra of unmodified and hydrogenated TiO_2 nanobelts. Inset: Tauc plot for the TiO_2 showing indirect gaps; (b) Micro-Raman spectra of unmodified and hydrogenated TiO_2 nanobelts. Inset: the most intense Eg peak of anatase TiO_2 for both, along with corresponding peak center positions and widths; (c) Photoluminescence spectra of unmodified and hydrogenated TiO_2 nanobelts.

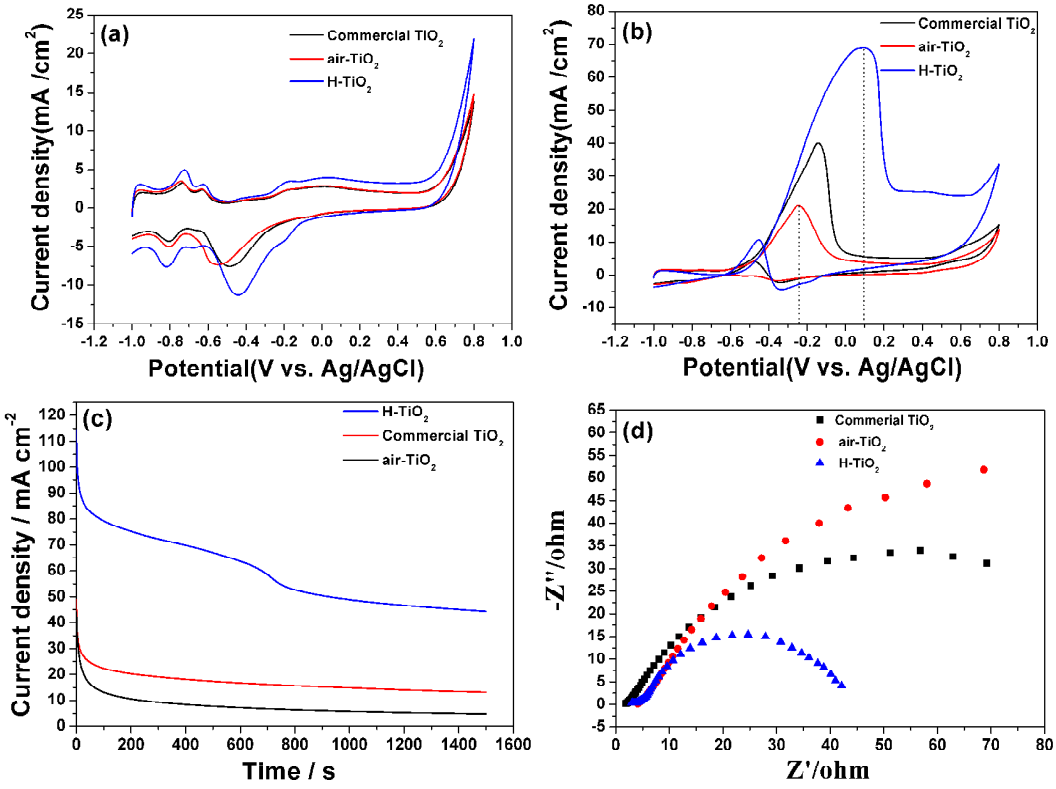

Figure 6 (a) CVs of the Pt/TiO_2/Ti electrode in 1.0 M NaOH aqueous solution at sweep rate of 50 mV s^{-1}; (b) CVs of the Pt/TiO_2/Ti electrode in 1.0 M NaOH aqueous solution containing 0.5 M methanol at sweep rate of 50 mV s^{-1}; (c) Amperometric I–t curves of the Pt/TiO_2/Ti electrode in 1.0 M NaOH aqueous solution containing 0.5 M methanol for 1500 s;(d) EIS and fitted plots of Pt/TiO_2/Ti electrode in a mixed solution of 1.0 M NaOH and 0.5 M methanol.

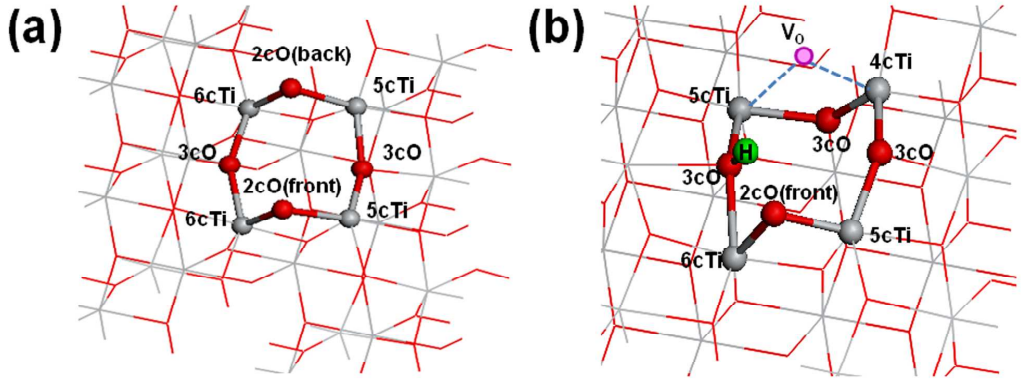

Figure 7 Top views of pure (a) and hydrogenated (b) anatase {101} surface. Ideal positions of the atoms before relaxation or removal are shown by blue dashed lines. The pink solid circle stands for the initial position of O atom before relaxation, and oxygen vacancy.

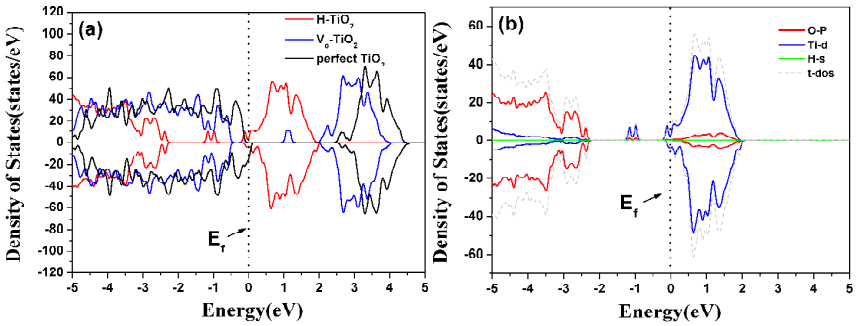

Figure 8 (a) the total density of states (TDOSs) of perfect TiO_2, oxygen vacancy TiO_2 and hydrogenated TiO_2; (b) the partial density of states (PDOS) of TiO_2 with hydrogen interstitial.

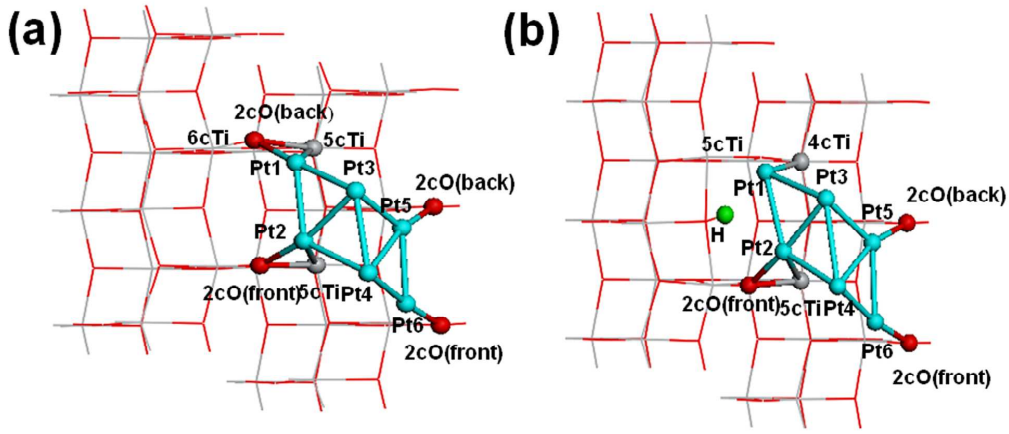

Figure 9 Top views of Pt_6 cluster adsorbed on pure (a) and hydrogenated (b) anatase {101}.

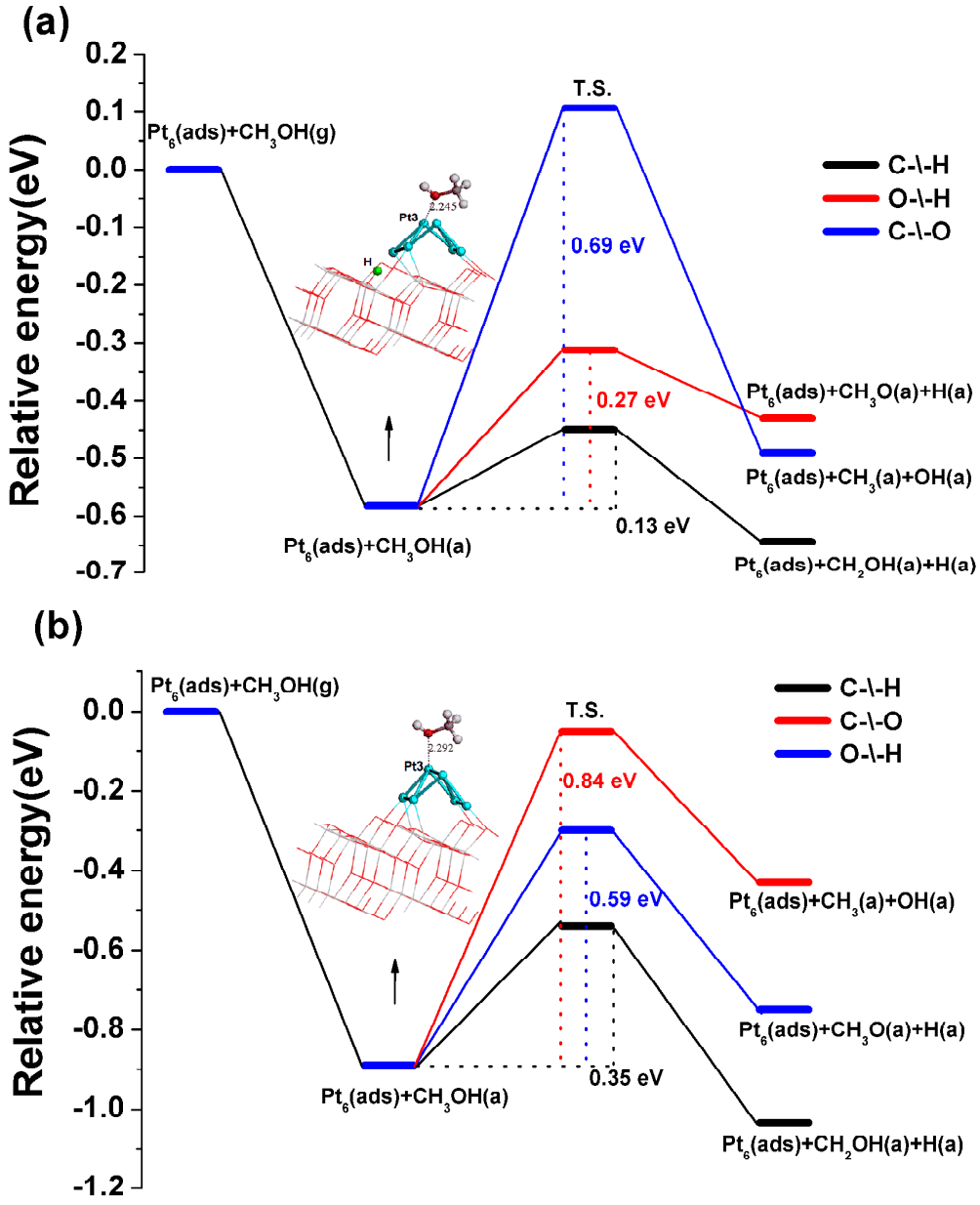

Figure 10 Potential energy profiles for CH_3OH dissociation starting from first bond scission over (a) Pt_6/H-TiO_2 and (b) Pt_6/TiO_2, respectively. The illustrations are CH_3OH adsorbed on Pt_6/ H-TiO_2 and Pt_6/ TiO_2, respectively.